

Supplementary information: Fibre multiwave-mixing combs reveal the broken symmetry of Fermi-Pasta-Ulam recurrence

Arnaud Mussot*, Corentin Naveau, Matteo Conforti, Alexandre Kudlinski, Francois Copie, and Pascal Szriftgiser*
Univ. Lille, CNRS, UMR 8523 - PhLAM - Physique des Lasers Atomes et Molécules, F-59000 Lille, France

Stefano Trillo†
Department of Engineering, University of Ferrara, Italy
(Dated: December 19, 2017)

DETAILS ON THE EXPERIMENTAL SETUP

A detailed sketch of the experimental setup (made of commercially available components) is depicted in Fig. S1. Three major challenges were faced to perform these recordings:

- (i) Phase locking of all laser sources involved in the experiments to perform relative phase measurements
- (ii) Fading phenomenon suppression. This temporal speckle like phenomenon occurs on the backscattered light from a quasi-monochromatic wave [1].
- (iii) Loss cancellation. Loss in the 7.7 Km long SMF-28, while relatively low (0.2 dB/km) would induce all the evolutions to drop on phase-shifted evolution [2], thus hiding the broken symmetry of FPU.

These three points, as well as the experimental setup are detailed below.

Fading suppression technique: In optical time domain reflectometry (OTDR), it is known that a random noise in amplitude and phase is superimposed on the backscattered light originating from variations of the state of the polarisation of the light and/or from local thermo-mechanical fluctuations of the scattering volume. Many efficient ways to avoid this additional source of noise have been developed by means of polarization scrambling techniques, integration over a huge number of backscattered signals, or frequency dithering of the light sources [3]. However, none of these techniques has been proven to be effective in our system and compatible with accurate distributed phase measurements. Thus, we have developed a technique almost immune to this detrimental effect. We make the reasonable assumption that the fading phenomenon is a purely linear effect with characteristic time scale greater than a few millisecond. Therefore, even if the linear response of the system is highly noisy and complex, it is however independent of the incoming power. We remove its contribution as follows. We launch two consecutive 50 ns pulses in the fibre. The first one is intense (450 mW) and is responsible for the nonlinear dynamics, whereas the second one is weaker, attenuated by 13 dB. The delay between them is set to 102 μ s. This delay is long enough to probe a fibre length up-to 10 km without overlap between two consecutive backscattered waves, but short enough compared to the characteristic response time of thermo-mechanical fluctuations, to ensure that gathered linear fading effect is strongly correlated for two consecutive pulses. Before going further, let us mention an important point. Thanks to two polarization beam splitters (PBS), we analyse each polarization states independently [4]. This has several advantages; there is no need for polarization scrambling which greatly reduce the acquisition time, and since all the contributions of both polarization states are known for the same shot, they can be recombined to further reduce the polarization fading effect. The principle of the measurement construction can be described as follows. Thanks to the heterodyne signals logged with the oscilloscope, the complex responses of each trace $A_{Pow,Pol,Channel}(Z)$ is demodulated (see below). Here, Z stands for the position along the fibre, the index Pow can either be *Strong* (for the nonlinear pulse), or *Weak* for the reference pulse, the index Pol is either 1 or 2 for each polarization state, and $Channel$ refers to as *pump* or *signal*. For instance, the pump response is evaluated by the two ratio $\frac{A_{Strong,1,Pump}(Z)}{A_{Weak,1,Pump}(Z)}$ and $\frac{A_{Strong,2,Pump}(Z)}{A_{Weak,2,Pump}(Z)}$.

Performing the ratio of these complex responses, cancels the fading effect in both amplitude and phase, revealing the non-linear response only. Without entering the full detailed procedure, the leading idea is to extract from these ratio the amplitude and phase of each polarization state, and to average them. The same is done for the signal side band.

A side effect of this method is that any linear contribution is lost (by construction). This includes the linear phase due to the group velocity dispersion acquired during the propagation. This contribution is linked to the linear phase mismatch term of the four-photon process underlying the MI process, and cannot be neglected. Consequently, it is included afterwards during the signal post-processing sequence. We add the following phase term $\frac{1}{2}\beta_2(2\pi f_m)^2 Z$ to the pump-signal phase difference to finally get $\Delta\phi$ that is used to represent experimental results in the main text (Figs. 3) and in Figs. S2. This new technique combined with an averaging over 200 shots gives an efficient suppression of the fading effect without significant impact on phase measurements.

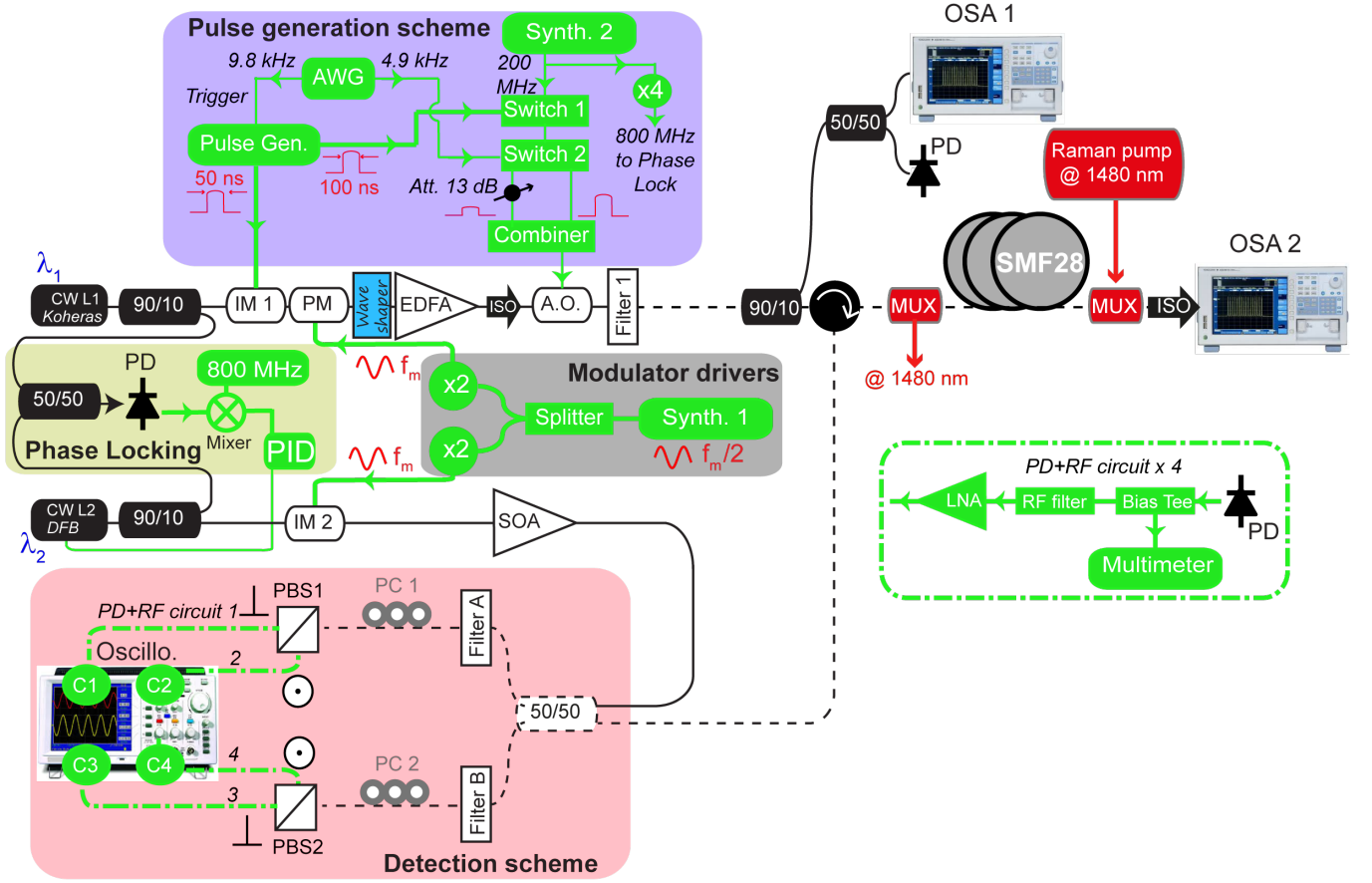


FIG. S1. Experimental setup. L1: narrow linewidth (100 Hz at FWHM) continuous wave laser of 47 mW; L2: continuous distributed feedback laser diode. L1 generates the pulses involved in the nonlinear process, L2 acts as a local oscillator for the heterodyne detection system. L2 is phase-locked with respect to L1 following the procedure described in Ref. [5]. Their beat-note is mixed with a 800 MHz reference. The resulting intermediate frequency drives the phase of L2 through a PID (proportional, integral, derivative) controller. IM(1,2): intensity modulator; PM: phase modulator. PM and IM2 generate sidebands at $f_m = 35$ GHz. To insure a fixed phase relation between them, they are driven by the same frequency doubled microwave source (Synth. 1). For information, all the instruments of the setup (including the oscilloscope) are referenced to the same 10 MHz clock. AWG: Arbitrary waveform generator; EDFA: erbium doped fibre amplifier; ISO: isolator; AO: acousto-optic modulator; PC: polarization controller; PBS: polarization beam splitter; PD: photo-detector; RF: radio frequency; LNA: low noise radio-frequency amplifier (1 dB noise figure); SOA: semi-conductor amplifier; MUX: multiplexer (or de-multiplexer) to inject (or remove) the Raman pump. Estimated insertion loss are: PBS: 0.7 dB; Filter A and B, 4.5 dB; Circulator, 0.8 dB; MUX 0.8 dB.

Raman amplifier: The losses of the SMF-28 are almost perfectly compensated by means of a scheme borrowed by telecommunication systems. The SMF fibre is pumped with a Raman laser source located at 1480 nm in the backward direction to minimize the relative intensity noise transfer from the pump to the signal [6]. A realistic simulation of this distributed Raman amplifier is complex to achieve due to the saturation of the Raman pump, the contra-propagation architecture and the relatively broad spectrum. Thus, we adjust the Raman pump power as follows. We choose the PM configuration ($\Delta\Phi_0 = \pi/2$) and increased the Raman pump power until the level of sideband power at the second recurrence ($z \approx 7$ km, see Fig. 3(d) in the main text) is similar to the first one ($z \approx 2$ km, see Fig. 3(d) in the main text). From the excellent agreement we obtained with numerical simulations we can infer that fibre losses are almost perfectly compensated in our system and that the fibre can be considered as fully transparent. Finally, when the Raman pump is off, we are not able to observe more than one period of recurrence or the homoclinic crossing, as in previous experiments.

Figures S2 display the phase portraits of the signal for different initial relative phase values $\Delta\phi_0 = 0, \pi/2, \pi$, and $3\pi/2$. Figures S2(a) to (d) have been obtained from numerical simulations of the NLSE with the parameters listed in Fig. 3 of the paper, whereas Figs. S2(e) to (h) reports the experimental measurements (note that Figs. S2(g,h) and (c,d) for numerical simulations, correspond to the two specific examples presented in Fig. 3 in the main paper). When

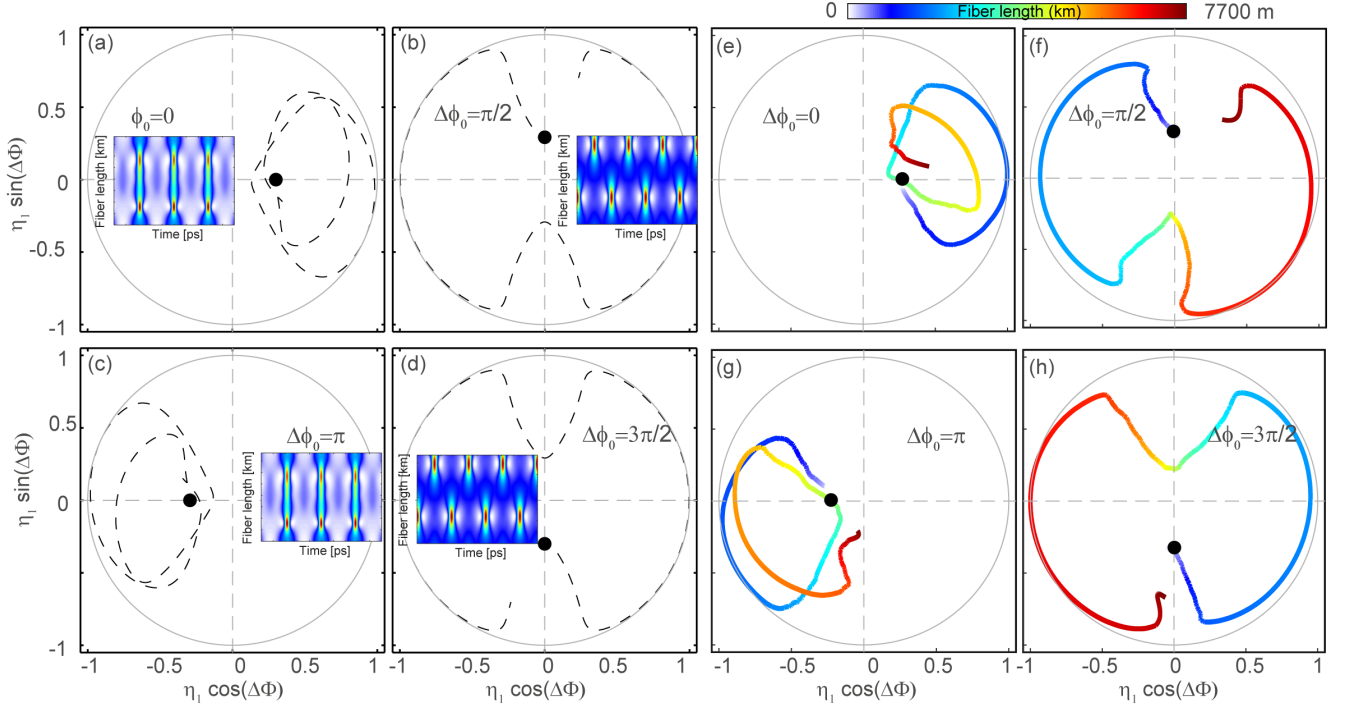


FIG. S2. Phase portraits of the signal for different relative initial phase values $\Delta\phi_0 = 0, \pi/2, \pi, 3\pi/2$. (a-d) Numerical simulations; (e-h) Experiments. The sideband power is normalized to its maximum value.

initial relative phase is $\Delta\phi_0 = \pm\pi/2$, the phase span the whole phase plane, and leads to a π phase shift of maximum recompression points in the time domain (see insets, from numerical simulations). Conversely, when $\Delta\phi_0 = 0, \pi$ the orbits remains confined in the right or left semi-plane ($-\pi/2 \leq \Delta\phi \leq \pi/2$), leading to in-phase recompression without temporal shift (see insets, from numerical simulations). In all cases, a good agreement is achieved between the experimental results (Figs. S2(e) to (h)) and the numerics (Figs. S2(a) to (d)).

Pulse generation: An arbitrary waveform generator (AWG) generates a clock at a 9.8 kHz rate, and another one at half this rate. The fastest clock triggers a pulse generator that delivers a 50 ns long pulse to drive the intensity modulator 1 (IM1). Then, the optical pulses pass through: a phase modulator (PM) to generate sideband waves at 35 GHz, an optical processor to statically control their relative phase (Waveshaper system), an erbium doped amplifier (EDFA) to reach a 440 mW peak power, and finally through an acousto-optic modulator (AO). This AO has a two-fold role. First, it increases the extinction ratio of the pulses to mitigate Stimulated Brillouin Scattering that would certainly be excited by a continuous optical leak between the pulses. Second, thanks to the half rate clock at 4.9 kHz, it attenuates one pulse over two to generate either the nonlinear pulse, or the reference one. Finally, the pulses are filtered out (Filter 1, bandwidth 1 nm FWHM) in order to remove the amplified spontaneous emission in excess.

Signal Processing: Each wave logged by the oscilloscope is demodulated with a short time Fast Fourier Transform (FFT). The wave is first sliced into segments made of 512 consecutive samples. Each segment has a 50 % overlap with the previous one to optimize the resolution. After the application of an Hamming window, the power and the relative phase at 600 MHz of each segment are evaluated with an FFT. Note: the demodulation is performed with a carrier centred at 600 MHz, and not at $\Delta F = 800 \text{ MHz}$. This is because one has to take into account the 200 MHz frequency shift induced by AO. Considering that the pulse width is 50 ns, one could expect a 5 meters resolution from this OTDR. However, due to the 512 points segment length, and considering the 2500 MHz sampling rate of the oscilloscope, the resolution is rather around 20 meters (to be compared to the 7.7 km fibre length). Considering some additional filtering steps described here after, this resolution is however further reduced. Indeed, all demodulated traces shown in the main paper and in Fig. S2 are obtained by averaging 200 recordings to remove the noise. For comparison, Fig. S3(a) shows a single shot of the relative phase $\Delta\phi(z)$ and Fig. S3(c) a collection of 50 recordings (grey curves). As can be seen on the single shot recording, the relative phase experiences π phase shifts that might be due to signal processing procedure used to extract the phase from raw data. It leads to significant variations from

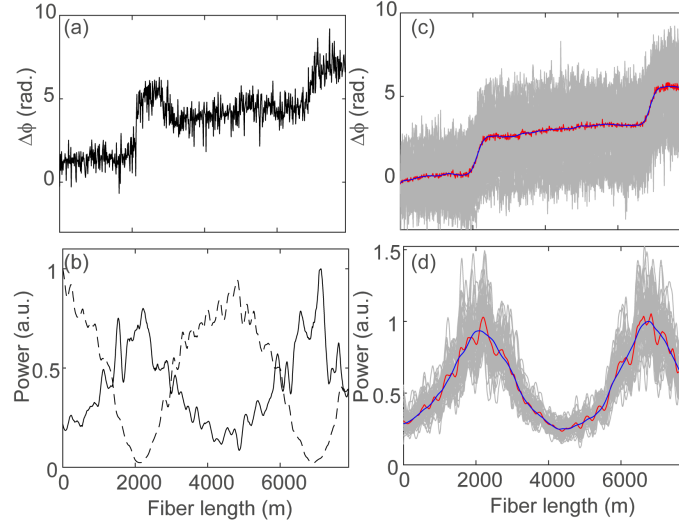


FIG. S3. Single shot recordings of (a) the relative phase $\Delta\phi$, (b) the pump (dashed line) and signal (solid line) powers. Collection of 50 consecutive recordings (grey) of (c) relative phase, and (c) of the signal power. (c) and (d) averaging (red curves) and smoothing with a Savitzky Golay filter (blue curves). It corresponds to $\phi_0 = \pi/2$ depicted in Figs. 3 (d)-(f) and Fig. S2 (h).

one recording to another that are suppressed by performing an averaging over a large number of shots (50, see red line in Fig. S3(c)). Small and rapid fluctuations are completely suppressed by means of a Savitzky-Golay filter (blue curve in Fig. S3(c)). Fig. S3(b) represents a single shot of the power evolution of the pump and sideband waves. It is quite remarkable to observe that the dynamics of the FPU recurrence process could be directly deduced from these raw data. Indeed, a clear two and half FPU recurrence cycle can unambiguously be seen from these traces with minima of the pump trace corresponding to maxima of the signal trace. As for the relative phase measurement, averaging and cleaning of the traces by means of a Savitzky-Golay filter (blue curve in Fig. S3(d)) allows to get a clean representation of these experimental results in the phase space that facilitate the comparison with numerical simulations without losing significant information on the dynamics. All these recording are driven with a computer and the typical time for one acquisition (200 recordings) is around 2 minutes.

Experimental procedure: In order to compare the impact of the input phase on phase-space trajectories, a critical point is to keep the optical power level launched along the fibre highly stable. For that purpose, at the beginning of each new acquisition, the sidebands generation is first shut off. A MI spectrum at the end of the fibre is logged by OSA2 and compared with a reference spectrum. If needed, the power is adjusted either by tuning the EDFA power, or for very fine adjustment, by tuning the RF level of synthesizer 2 (it has a 0.01 dB resolution and no thermal effect) by looking at the level of MI side lobes at the perfect phase matching frequency since it is very sensitive to pump power fluctuations (exponential at this frequency shift). The sidebands generation is then switched on and a reference spectrum is recorded. The time of flight sequence as described above is then performed. After that, at the end of the recording, two other spectra (sidebands on and off) are acquired and compared again to their respective reference spectra acquired at the beginning of the sequence. This allows us to check that no measurable power drift occurred during the acquisition. This procedure is systematic and highly effective. With no time limitation, we estimate that it allows for a stabilization of the launched power with a reproducibility better than 2%.

Brillouin scattering/Noise Limitation: Figure S4 shows the spectrum of the backscattered light when Raman pump is on by launching powerful pulses only to get absolute power measurements of waves involved in the FPU recurrence process. This measurement is performed just at the output of the circulator. First, one can see Brillouin scattering sidebands at 10.9 GHz around each optical component involved in the FPU recurrence process. The level of these sidebands is very weak, 16.5 dB below the backscattered pump for instance. This means that their absolute level is several orders of magnitude below the pump power, and that stimulated Brillouin scattering is completely negligible in this experiment (spontaneous and not stimulated). Second, the fact that the Stokes and anti-Stokes bands shifted from ± 10.92 GHz from each FPU component are symmetric also confirms that this spectrum correspond to spontaneous Brillouin scattering. A stimulated spectrum would be strongly asymmetric with a powerful Stokes band due to Brillouin gain. Furthermore, there is an important background compared to the noise floor of the OSA that is mostly due to Raman amplification used to compensate the loss. While the contra-propagative Raman pump scheme

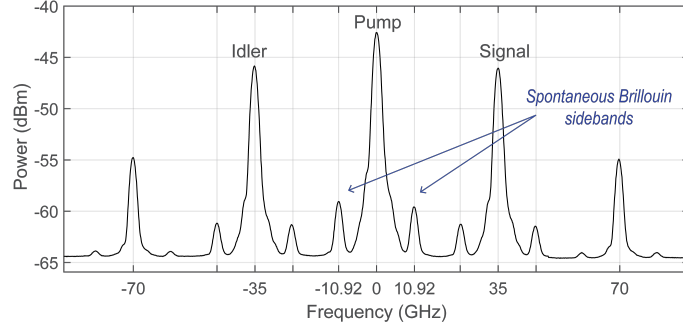


FIG. S4. Backscattered spectrum recorded at the output of the circulator by launching only strong pulses (no fading correction).

strongly reduces the amount of noise transferred on forward signals, it is quite important on the backscattered one. The noise power is around -64 dBm for the 2.5 GHz OSA resolution. The bandwidth of the final detection at 600 MHz is around 10 MHz. Within this bandwidth, the Raman noise power is reduced to -88 dBm. Considering that, this noise has a random polarization, the Raman noise power received by the optical detector is around -99 dBm. To give a comparison, the ultimate signal to noise ratio limitation of the experiment is presently the electrical thermal noise power of the detectors, $P_{Nyquist}$. At room temperature $P_{Nyquist} = -174 + 10 \log_{10}(\Delta f)$. With $\Delta f = 10$ MHz, and assuming a 1 dB amplifier noise figure, the thermal noise is at a -103 dBm level. Thus, Raman noise is above this level and does not affect significantly our measurements.

EXACT SOLUTIONS OF THE NLSE

In principle both the phase-unshifted and phase-shifted evolutions can be described by doubly-period solutions of the NLSE. Solutions of this kind have been reported originally in Ref. [7, 8] and discussed again in Ref. [2] with reference to the interpretation of a hydrodynamic experiment in deep water (note, however, that in Ref. [2], only phase-shifted evolutions generated from a weakly modulated carrier are observed due to the fact that the experiment is conducted in the regime dominated by the losses). For sake of completeness, we report such solutions also here, with reference to the NLSE in normalized units as

$$i \frac{\partial \psi}{\partial z} + \frac{1}{2} \frac{\partial^2 \psi}{\partial t^2} + |\psi|^2 \psi = 0. \quad (S1)$$

The first solution of Eq. (S1) describing unshifted evolution reads

$$\psi(z, t) = \frac{k}{2} \frac{A(t) \text{cn}(z/2, k) + i \sqrt{1+k} \text{sn}(z/2, k)}{\sqrt{1+k} - A(t) \text{dn}(z/2, k)} \exp\left(i \frac{z}{2}\right), \quad A(t) = \frac{\text{cn}\left(\sqrt{\frac{1+k}{2}} t, \sqrt{\frac{1-k}{1+k}}\right)}{\text{dn}\left(\sqrt{\frac{1+k}{2}} t, \sqrt{\frac{1-k}{1+k}}\right)}, \quad (S2)$$

whereas the solution describing evolutions with shift reads

$$\psi(z, t) = \frac{\sqrt{\frac{k}{1+k}}}{\sqrt{2}k} \frac{\text{cn}\left(\frac{t}{\sqrt{k}}, \frac{1-k}{2}\right) \text{dn}\left(\frac{z}{2k}, k\right) + i \text{sn}\left(\frac{z}{2k}, k\right)}{1 - \frac{k}{1+k} \text{cn}\left(\frac{t}{\sqrt{k}}, \frac{1-k}{2}\right) \text{cn}\left(\frac{z}{2k}, k\right)} \exp\left(i \frac{z}{2}\right). \quad (S3)$$

They both depend on a single parameter k , which jointly fixes both the longitudinal period of the evolution and the temporal period of the modulation T_m or equivalently the frequency $\omega = 2\pi/T_m$. Figures S5(a,b) show how the solutions in Eqs. (S2-S3) look like in the evolution. The important point that we emphasize here is that they cannot describe our experiment for two fundamental reasons: (i) they cannot describe the homoclinic crossing at constant modulation frequency ω . In fact, as shown in Fig. S5(c), their characteristic temporal frequency ω as a function of the parameter k is always different except in the limit $k \rightarrow 1$ where $\omega \rightarrow 1$. In this limit, however, the spatial period of the solutions diverges, and both solutions describe the Akhmediev breather (homoclinic loop or separatrix of the MI) instead of the recurrent dynamics. In particular note that the unshifted solution is valid for low frequencies that

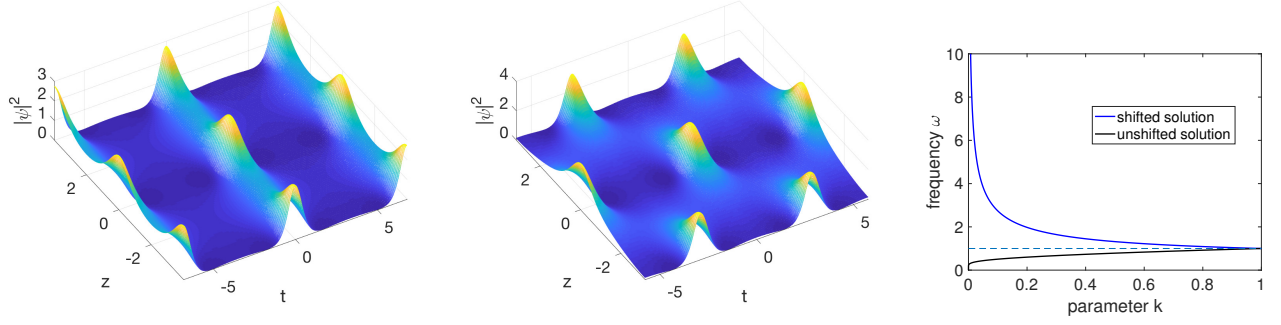


FIG. S5. Exact doubly-periodic solutions of the NLSE. (a) 3D plot of the recurrent solution that exhibits no shift in time; (b) Same for the solution that exhibits shift in time. Here $k = 0.8$ in both cases. (c) dependence of the normalized modulation frequency $\omega = 2\pi/T_p$ (T_p is the temporal period of the solution) as a function of the parameter k , for the two types of solutions.

lie within the MI spectral gain bandwidth, whereas the shifted solution features mostly high frequencies outside the MI gain bandwidth, i.e. the stable regime; (ii) in the experiment, by operating at fixed frequency, the longitudinal spatial period shows a marked dependence on the initial depth of modulation, a feature that cannot be described by these solutions.

The homoclinic crossing that leads to switch between an unshifted (inner, Fig. 1(c,f) in the text) orbits and shifted (outer, Fig. 1(d,g) in the text) orbits has also been characterized, exploiting the integrability of the NLSE, in terms of the periodic inverse scattering [9]. According to this picture the homoclinic loop or separatrix (Akhmediev breather, Fig. 1(e,h)) corresponds to an eigenvalue double point lying on the imaginary axis. When moving towards inner or outer doubly periodic orbits, this double point splits in the complex plane. In particular, for inner orbits, the split occurs on the imaginary axis, thus creating a gap. Conversely, for outer orbits the split occurs in orthogonal direction creating a cross state. In spite of this understanding, however, it remains extremely challenging to construct more general doubly periodic solutions of the NLSE that describe the homoclinic crossing observed at constant modulation frequency under experimental conditions. To the best of our knowledge, they have not been reported in the literature yet.

On the other hand, the three-wave truncation provides a simple, accurate, and practical approach that allows for capturing the essential physics of the problem, at least when there is only one unstable mode (i.e., $1 \leq \omega \leq 2$). In the next section we discuss in more details the topologies of the phase-plane associated with the three-wave truncation and the general condition for homoclinic crossing.

PHASE-PLANE STRUCTURE AND GENERAL CONDITIONS FOR HOMOCLINIC CROSSING

We highlight the fact that the homoclinic structure which represents the continuation of the MI into the depleted regime and which is responsible for the broken symmetry of the FPU recurrences, appears as soon as the normalized modulation frequency ω changes across the onset for MI at $\omega = 2$. The deep qualitative change of the topology of phase-space which is associated with this transition can be appreciated by contrasting Fig. S6(a) (modulationally stable case $\omega > 2$) and Fig. S6(c) (modulationally unstable case, $\omega < 2$), which reports the level curves of the Hamiltonian of the 3WM process in the cartesian phase plane $(x, y) = (\eta_1 \cos \Delta\phi, \eta_1 \sin \Delta\phi)$. For completeness, in Fig. S6(b,d) we also show the corresponding topologies in the phase-plane of polar coordinate $(\Delta\phi, \eta_1)$.

Figure S6(a,c) show that the modulationally stable case is characterized by orbits which describe very weak periodic conversions, without any interesting phase-plane structure. Conversely, for $\omega < 2$, a separatrix or homoclinic loop appears (black solid curve in Fig. S6(b,d)), which divides the phase-plane into different domains corresponding to the qualitatively different dynamics discussed in the text. We point out that that we stick to the more common terminology of homoclinic structure' used in the literature, though the separatrix is, strictly speaking, a heteroclinic loop since it connects $\eta_1 = 0$ (i.e., the pump mode) with itself with opposite phases $\Delta\phi = \pm\Delta\phi_c$, in a fully consistent way with the exact solution known as Akhmediev breather which is the separatrix in the full NLSE [7, 8]. The values $\Delta\phi = -\Delta\phi_c$ and $\Delta\phi = \Delta\phi_c$ constitute the unstable manifold (i.e., characterized by growing modulations) and the stable manifold (i.e., characterized by decreasing modulations) of the saddle point $\eta_1 = 0$ from which the separatrix emanates (see Fig. S6(d), where $\Delta\phi_c = \pi/4$). Equivalently, in the cartesian representation of Fig. S6(b) $\Delta\phi = \pm\Delta\phi_c$ fix the slopes of the separatrix around the origin. The value of phase $\Delta\phi_c$ is extremely important because it fixes the

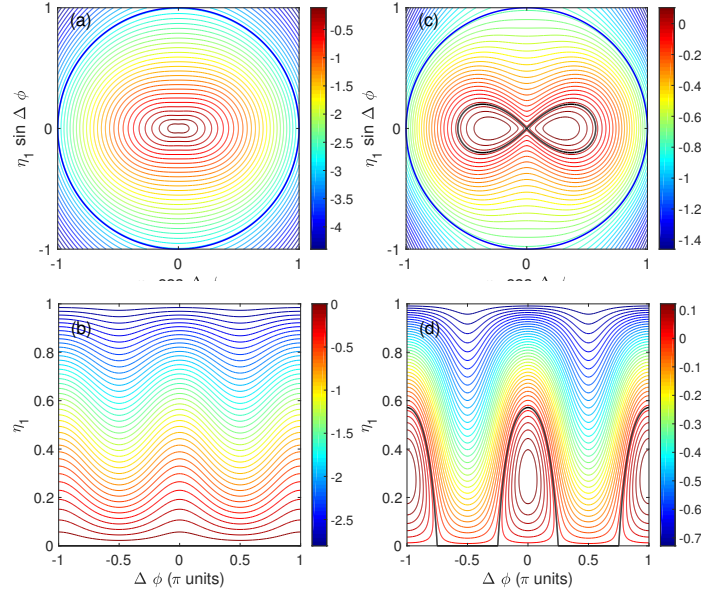


FIG. S6. Change of topology in the 3WM phase plane when going through the onset of MI. Left column (a,b): the modulationally stable case, $\omega = 2.5$; Right column (c,d): the modulationally unstable case, $\omega = \sqrt{2}$, corresponding to peak MI gain. (a,c) phase plane in cartesian coordinates $(x, y) = (\eta_1 \cos \Delta\phi, \eta_1 \sin \Delta\phi)$; (b,d) equivalent phase plane in polar coordinates $(\Delta\phi, \eta_1)$.

boundaries, in the limit of very weak (ideally vanishing) modulation, across which abrupt switching occurs between shifted and unshifted orbits, owing to separatrix crossing. In particular unshifted evolutions are obtained for initial conditions either in the range $-\Delta\phi_c \leq \Delta\phi_0 \leq \Delta\phi_c$ (single loop orbits around $\Delta\phi = 0$, e.g. case of Fig. S2(a,e)) or in the range $\pi - \Delta\phi_c \leq \Delta\phi_0 \leq \pi + \Delta\phi_c$ (single loop orbits around $\Delta\phi = \pi$, e.g. case of Fig. S2(c,g)), whereas phase-shifted evolutions correspond either to $\Delta\phi_c \leq \Delta\phi_0 \leq \pi - \Delta\phi_c$ or $\Delta\phi_c - \pi \leq \Delta\phi_0 \leq -\Delta\phi_c$ (double loop orbits corresponding e.g. to the case of Fig. S2(b,f) or Fig. S2(d,h), respectively).

Importantly, the critical value of the phase $\Delta\phi_c$, and hence the above conditions, depend on the modulation frequency. This can be seen by searching for the coordinates of the saddle by imposing $d\Delta\phi/dz = d\eta_1/dz = 0$. The value $\Delta\phi = \Delta\phi_c$ which fulfils $d\Delta\phi/dz = 0$, subject to the condition $\eta_1 = 1$ (i.e., the pump, that guarantees $d\eta_1/dz = 0$), is easily obtained in closed form as $\Delta\phi_c = \cos^{-1}(\omega/2)$. Therefore $\Delta\phi_c$ ranges from $\Delta\phi_c = 0$ at the onset of MI ($\omega = 2$) to $\Delta\phi_c = \pi/2$ at $\omega = 0$, as illustrated in Fig. S7(a) (we warn, however, about the fact that for $\omega < 1$, higher-order MI can take place, which involves more complicated separatrices that are not addressed in this work). As an important consequence, we emphasize that the cardinal phases $\Delta\phi_0 = 0, \pi/2, \pi, 3\pi/2$ that we have focused on, play a special role, being the most robust and less critical input phases. Indeed the initial conditions $\Delta\phi_0 = 0, \pi$ and $\Delta\phi_0 = \pi/2, 3\pi/2$ always lead to unshifted and shifted orbits, respectively, regardless of the specific value of ω and hence of the main parameters (modulation frequency and power). Therefore passing from $\Delta\phi_0 = 0$ (or $\Delta\phi_0 = \pi$) to

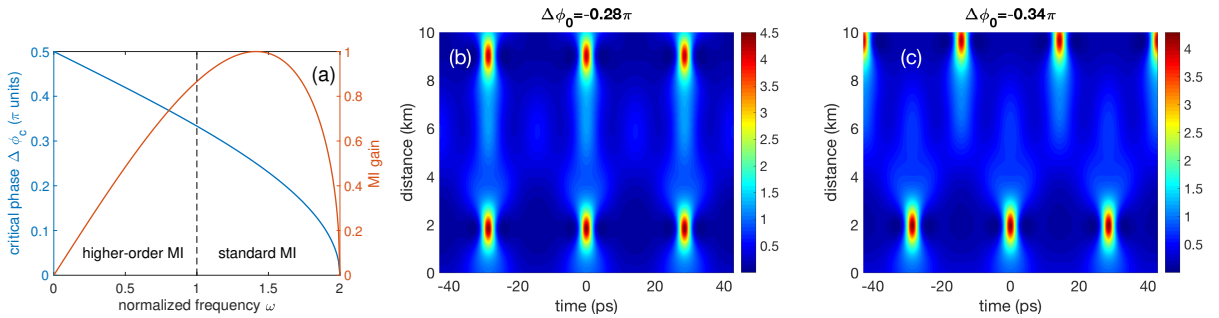


FIG. S7. (a) Critical phase $\Delta\phi_c$ vs. ω , with superimposed MI gain. The dashed vertical line divides the region of standard MI (only one unstable sideband pair) of interest here from higher-order MI ruled by more complicated separatrices (higher-order Akhmediev breathers). (b,c) NLSE simulations showing the power evolutions obtained when the input phase is changed (as indicated on the panels) across the critical value. All parameters as in Fig. 4 of the paper, except $P_p/P_s = 10$ dB.

$\Delta\phi_0 = \pi/2$ (or equivalently $\Delta\phi_0 = 3\pi/2$) always lead to switch via homoclinic crossing.

When the modulation is relatively strong, a critical phase for switching still exist, which need to be determined numerically, presenting small deviations from the 3WM value valid in the limit of vanishing modulation. This is shown for instance in Fig. S7(b,c) where we change the input phase across the critical value $\Delta\phi = -\Delta\phi_c \simeq -0.31\pi$ (to be compared with the limit value from 3WM $\Delta\phi = -\Delta\phi_c \simeq -0.29\pi$).

We have also performed measurements to report evidence for such type of switching around the critical phase. This further increase the difficulty of the experiment because, when approaching the separatrix, the spatial period tends to diverge. Indeed we have found that the 7.7 km fiber was too short to report such evidence. In this case we have employed a longer span (9.2 km) of exactly the same SMF28, at the price of the fact that the Raman compensation scheme is no longer optimum for such length. Figure S8 displays the power and phase evolutions as well as the phase-

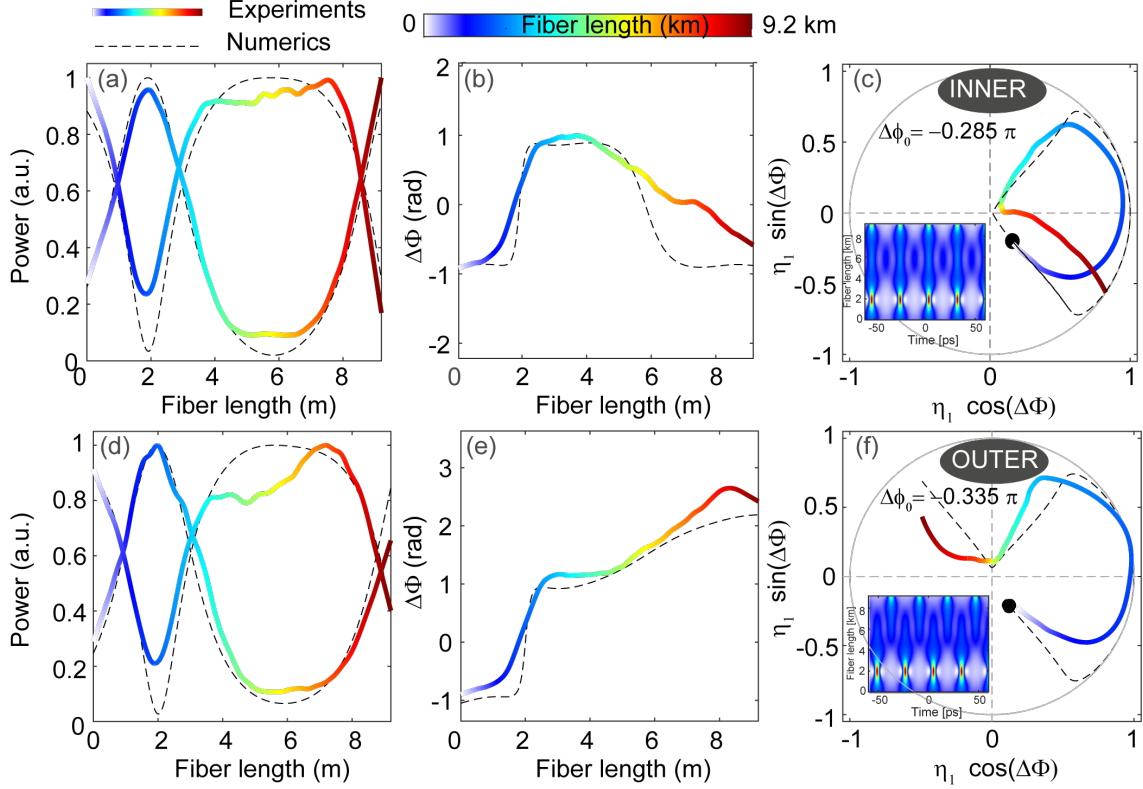


FIG. S8. Evolution along the fibre length of (a,d) the pump power and the first sideband pair power; (b, e) the relative phase $\Delta\phi(z)$. (c,f) Projections of the evolutions in the 3WM phase plane (the insets show the expected evolutions). Numerical simulations are depicted in black dashed lines and experiments in solid rainbow lines. (a, b, c) and (d, e, f) differ only for the initial relative phase of the modulation $\Delta\phi_0 = -0.285\pi$ (inner trajectory) and $\Delta\phi_0 = -0.335\pi$ (outer trajectory), respectively. Parameters as in Fig. S2 except for $L = 9.2$ km and pump-signal power ratio equals to 10.5 dB. All power plots are normalized to their respective maxima.

plane projections when the phase is changed by nearly 15% (from $\Delta\phi_0 = -0.285\pi$ to $\Delta\phi_0 = -0.335\pi$). While the power evolutions look similar, a clear difference exists in the phase evolutions and the phase-plane projections between the two cases. Figure S8 (a, b, c) showcases an inner trajectory while Figure S8 (d, e, f) an outer one. The initial phase has been changed by the smallest amount ($\Delta\phi_0 = 0.05\pi$) that allows to observe this behavior experimentally in a reproducible way. It is important to point out that the switching dynamics of the system, characterized by inner or outer trajectories is extremely sensitive to any parameter variations when working close to the separatrix. Finally, though we have chosen to evidence the switching process by changing the initial phase value, in principle, it might be possible to achieve switching also by tuning the perturbation amplitude only (i.e. the sideband amplitude). However, this requires to operate very close to the critical phase and to have a large excursion in amplitude (the variation of the initial condition occurs in the vertical direction in the phase plane shown in Fig. S6(d), nearly parallel to the separatrix). In particular, this excursion is too large concerning what can be performed with our present experimental setup. Further investigations with a modified setup are required to report it experimentally in an unambiguous way.

* arnaud.mussot@univ-lille1.fr

† stefano.trillo@unife.it

- [1] P. Healey, Fading in heterodyne OTDR, *Electron. Lett.* **20**, 30-32 (1984).
- [2] O. Kimmoun, H.C. Hsu, H. Branger, M.S. Li, Y.Y. Chen, C. Kharif, M. Onorato, E. J. R. Kelleher, B. Kibler, N. Akhmediev, and A. Chabchoub, Modulation Instability and Phase-Shifted Fermi-Pasta-Ulam Recurrence, *Sci. Rep.* **6**, 28516 (2016).
- [3] H. Izumita, S. Furukawa, Y. Koyamada, and I. Sankawa, Fading noise reduction in coherent OTDR, *IEEE Phot. Tech. Lett.* **4**, 201-203 (1992).
- [4] G. Yang, X. Fan, B. Wang, Q. Liu, and Z. He, Polarization fading elimination in phase-extracted OTDR for distributed fiber-optic vibration sensing, *OptoElectronics and Communications Conference (OECC)*, (2016).
- [5] F. Friederich, G. Schuricht, A. Deninger, F. Lison, G. Spickermann, P. H. Bolívar, and H. G. Roskos, Phase-locking of the beat signal of two distributed-feedback diode lasers to oscillators working in the MHz to THz range, *Opt. Express* **18**, 8621-8629 (2010).
- [6] C. Headley and G. P. Agrawal, *Raman Amplification in fiber optical communication systems*, (Academic Press, Amsterdam, 2005).
- [7] N. N. Akhmediev, V.M. Eleonskii, and N.E. Kulagin, Generation of periodic trains of picosecond pulses in an optical fiber: exact solutions, *Sov. Phys. JETP* **62**, 894 (1985); N.N. Akhmediev, V.M. Eleonskii, and N. E. Kulagin, Exact first-order solutions of the nonlinear Schrödinger equation, *Theor. Math. Phys. (USSR)* **72**, 809 (1987).
- [8] N. N. Akhmediev and Ankiewicz, *Solitons: Non-linear pulses and beams* (Chapman and Hall, 1997)
- [9] M. J. Ablowitz, B. M. Herbst, and C.M. Schober, Computational chaos in the nonlinear Schrödinger equation without homoclinic crossings, *Physica A* **228**, 212 (1996).